Progress In Electromagnetics Research C, Vol. 136, 137–149, 2023

Super-Wideband Fractal Antenna for Future Generations of Wireless Communication

Mohamed S. Fouad[1, 3], Asmaa E. Farahat[2], Khalid F. A. Hussein[2, *], Abdelhamid A. Shaalan[3], and Mai F. Ahmed[3]

Abstract—A super-wideband (SWB) antenna of enhanced performance is proposed to cover the frequency band from 3 to 30 GHz. The proposed antenna can be regarded as a two-arm antenna of fractal structure. Each of the antenna arms can be viewed as composed of multiple merged wideband fractal elements. Each fractal element is a wide-flare metallic sector-shaped radiator with circular (arc-shaped) edges to enhance the bandwidth over which the antenna impedance is matched to 50 Ω-feeder. A novel SWB balun is proposed for feeding the two-arm antenna of its balanced structure through the conventional coaxial feeder of its unbalanced structure. For experimental assessment of its performance, the proposed antenna is fabricated and measured by a vector network analyzer (VNA). The experimental results come in agreement with the results obtained by the CST® simulator. It is shown that the proposed antenna has a ratio bandwidth (RBW) of 10 : 1, percentage bandwidth (%BW) of 164%, and bandwidth-dimension ratio (BDR) of 1952. The efficiency of radiation of the proposed antenna is shown to be greater than 98% over most of the operational frequency band.

1. INTRODUCTION

The enormously growing number of users and the increasing demand for higher data rate and spectral efficiency in mobile networks necessitate the employment of compact, multifunctional, multiband, and wideband antennas with high performance [1–5]. The frequency range (3.1–10.6 GHz) is allocated for the ultra-wideband (UWB) communication. However, the super-wideband (SWB) operation does not have specific limits of the operational frequency range like the UWB operation. The antennas that have ratio bandwidth (RBW) of at least 10 : 1 for impedance matching (i.e., the magnitude of its reflection coefficient is less than or equal to −10 dB) are considered as SWB antennas. WB technology has more advantages than UWB as it provides a larger frequency range. Because of their limitations of low power and relatively slow response to adaptation and signal acquisition, UWB antennas may not be able to operate with high performance for long range wireless communications [1–9]. The wider frequency band of SWB antennas in comparison to UWB antennas enables their operation for wider categories of wireless applications including both short-range and long-range communication. A single SWB antenna can operate simultaneously for multiple operational frequency bands that are required for future mobile communication [1–9]. Moreover, compared to UWB, SWB technology offers a larger channel capacity in communication, superior resolution in screening, and higher precision with greater time-accuracy in ranging [1–9]. For the above reasons, the present work proposes a two-arm SWB antenna as a good candidate for future generations of mobile communications as it can overcome the shortcomings in the performance of UWB antennas.

Received 25 April 2023, Accepted 25 July 2023, Scheduled 16 August 2023
* Corresponding author: Khalid Fawzy Ahmed Hussein (fkhalid@eri.sci.eg).
[1] High Institute of Electronic Engineering, Belbis, Egypt. [2] Department of Microwave Engineering, Electronics Research Institute (ERI), Cairo 11843, Egypt. [3] Department of Electronics and Communication Engineering, Faculty of Engineering, Zagazig University, Zagazig, Egypt.

In the recent publications, a little work has been interested in the SWB antenna design. The main challenge to design an SWB antenna is to maintain a very wide frequency band (with RBW of at least 10 : 1) using an antenna of small size as required by most of the recent and future applications. A patch antenna shaped like a bowtie with some modifications is proposed in [3] to cover the operation over the frequency band 3.03–17.39 GHz. This antenna is fed through a coplanar waveguide (CPW) with asymmetric ground sides. A circular disc is proposed in [4] to operate as an SWB antenna over the frequency range 2.7–28.8 GHz. Two stepped feed lines are employed for the design of this antenna. In [5], a hexagon-shaped patch with double slots is proposed as an SWB to cover the frequency band 3.4–37.4 GHz. This patch is fed through CPW to have a coplanar structure. A patch that is shaped like an octagonal-ring is proposed in [6] to cover the frequency range 2.59–31.14 GHz. The feed line of this patch is shifted off the axis of symmetry with a notch that is etched in the ground structure. A patch of a steering-wheel shape is proposed in [7] as SWB antenna to cover the frequency range 2.3–34.8 GHz. To enhance the bandwidth, this patch is placed over a partial ground area of round corners and with a notch in each corner.

An SWB two-arm antenna with a fractal structure is proposed in the present work to cover the frequency band (3–30 GHz). This requires the radiating elements and feeding mechanism (transition between the coaxial feeder and the radiator) to efficiently support the operation over such very wide band of the frequency. A novel antenna design is introduced for extending the bandwidth and enhancing the antenna efficiency by proposing the fractal antenna structure as multiple merged wide-flare sectorial metallic radiators with arc-shaped edges. A wideband balun is proposed for excitation of the balanced antenna structure through a coaxial line.

The present paper comes in seven sections. After the introduction, The proposed antenna design is described in Section 2. The antenna fabrication and the measurement of the reflection coefficient are presented in Section 3. The far field patterns are presented and discussed in Section 4. The results concerned with the antenna gain and efficiency are presented in Section 5. The comparative performance assessment regarding the SWB antennas presented in some recent publications is discussed in Section 6. Finally, Section 7 provides a summary of the most important conclusions of the present work.

2. DESIGN OF THE PROPOSED ANTENNA

The present section provides detailed explanation of the design of a super-wideband radiating antenna structure as well as the design of the wideband feeding balun.

2.1. Antenna Structure

The principle of being capable of achieving SWB operation is to get the proposed two-arm antenna constructed as a fractal antenna. Each arm of the antenna can be seen as composed of multiple (fractal) elements that are merged in one structure. Each fractal element is a wideband sector-shaped metallic radiator of circular arcs and wide center (flare) angle. Five merged circular sectorial radiators are proposed to construct the antenna arms as shown in Figure 1. The sectorial elements have increasing radii and decaying flare angles when moving from the innermost element to the outermost one.

The flare angles and the radii of the sectorial metallic radiators are, respectively, calculated as follows.

$$\psi_n = \psi_0 - n\Delta\psi, \quad n = 1, 2, ..., 5 \tag{1}$$

$$R_n = R_0 + n\Delta R, \quad n = 1, 2, ..., 5 \tag{2}$$

where n is the index of the sectorial radiator ordered from the innermost to the outermost.

The values of Ψ_0, $\Delta\psi$, R_0, and ΔR should be selected to get the best antenna performance.

2.2. Wideband Feeding Balun

The proposed two-arm antenna has a balanced structure and is to be excited through a coaxial line of an unbalanced structure. Therefore, a broadband balun is required for this purpose. The split coaxial balun introduced in [10] and [11] is the most common balun that can be used for feeding the balanced

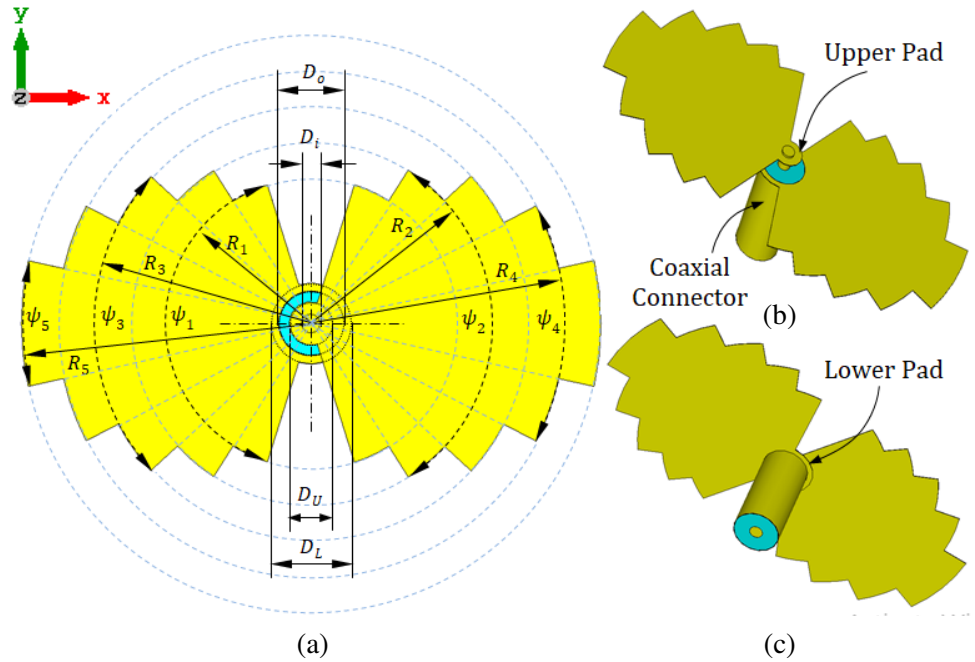

Figure 1. Design of the SWB antenna of two-arm structure. (a) Top view. (b) 3D view showing the antenna top. (c) 3D view showing the antenna bottom.

two-arm antennas through a coaxial line. It can be considered as the nearest one to the balun proposed in the present work. However, such split coaxial balun has a three-dimensional structure and is not appropriate for feeding the SWB two-arm antenna presented in Figure 1. A balun with quasi-planar structure that is compact and suitable for printed and free-standing two-arm antennas is introduced in this section. Figure 1 shows the structure of the proposed balun attaching the coaxial launcher to the antenna arms. The outer conductor of the coaxial launcher is attached to the lower antenna arms through a ring of outer diameter D_L. The inner conductor of the coaxial launcher is extended as a probe of length L and is attached to the upper antenna arm through a circular ring of outer diameter D_R. Thus, the proposed balun is constructed as two circular rings and a probe extension. The diameters ratio D_L/D_U and the probe length, L, control the frequency band of impedance matching.

A complete parametric study has been performed to determine the best values of the antenna design parameters in order to realize the required bandwidth (3–30 GHz) and to maximize the antenna efficiency. It has been found that the best parameters are $R_0 = 7.5\,\text{mm}$, $\Delta R = 2.5\,\text{mm}$, $\psi_0 = 175°$, and $\Delta\psi = 30°$. Consequently, $R_1 = 10\,\text{mm}$, $R_2 = 12.5\,\text{mm}$, $R_3 = 15\,\text{mm}$, $R_4 = 17.5\,\text{mm}$, $R_5 = 20\,\text{mm}$, $\psi_1 = 145°$, $\psi_2 = 115°$, $\psi_3 = 85°$, $\psi_4 = 55°$, and $\psi_5 = 25°$. The antenna dimensions that satisfy the design objectives are given in Table 1.

Table 1. Dimensions of the SWB two-arm antenna with the structure shown in Figure 1.

Parameter	R_0	ΔR	L	D_U	D_L	D_o	D_i	Parameter	Ψ_0	$\Delta\Psi$	ϵ_r
Value (mm)	7.5	2.5	1.5	3.0	5.6	4.45	1.3	Value	175°	2.5	2.0

2.3. Setting the Antenna Design Parameters through Parametric Study

In this section, the best values of design parameters shown in Figure 1 for the optimal performance of the proposed antenna are obtained through parametric studies. Actually, the numerical investigations presented here are only some examples selected from a more complete parametric study that has been performed for the best design of the proposed antenna.

The frequency response of $|S_{11}|$ is affected by changing the longest radius, R_5, as shown in Figure 2. It is clear that the start frequency of the impedance matching band decreases with increasing R_5. However, the widest frequency band and maximum RBW are obtained when $R_5 = 20\,\text{mm}$ as shown in the figure.

When the incremental length, ΔR, of the sectorial fractal elements changes it affects the frequency behavior of the reflection coefficient at the antenna port as depicted in Figure 3. The start of the frequency band seems insensitive to the variation of ΔR; however, the upper frequency is significantly affected by this dimensional parameter. It is shown that setting $\Delta R = 2.5$ gives the largest frequency band and the highest RBW.

The variation of the reference flare angle, Ψ_0, of the sectorial fractal elements affects the frequency response of the $|S_{11}|$ as shown in Figure 4. The start of the frequency band seems unaffected by the variation of Ψ_0. On the other hand, the end of the frequency band is strongly dependent on this parameter. It is evident that setting $\Psi_0 = 175^\circ$ results in the widest frequency band and the best RBW.

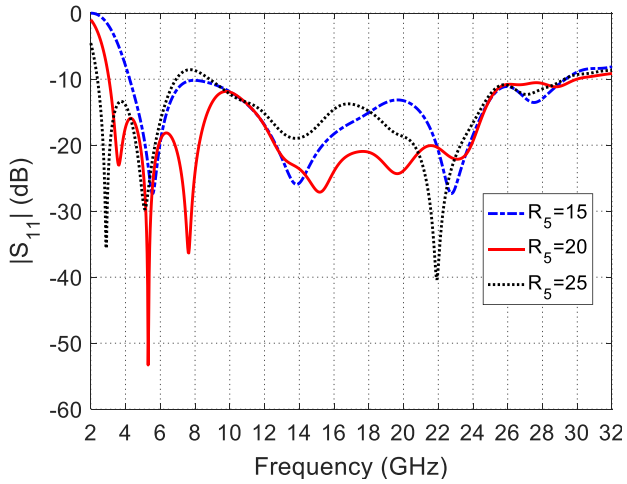

Figure 2. Effect of varying the arm length, R_5, on the frequency response of $|S_{11}|$.

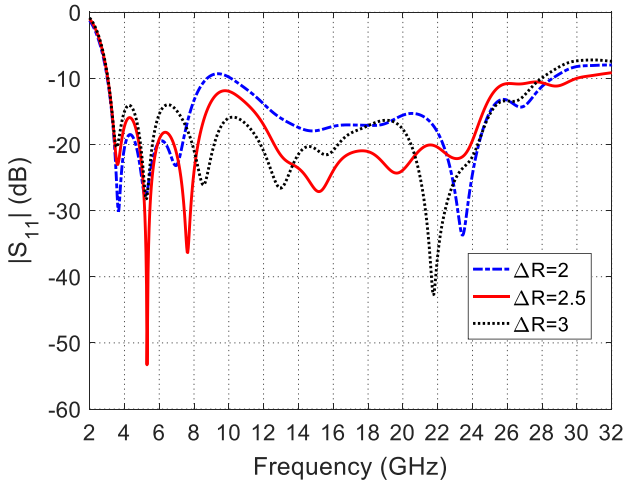

Figure 3. Effect of varying the incremental length, ΔR, on the frequency response of $|S_{11}|$.

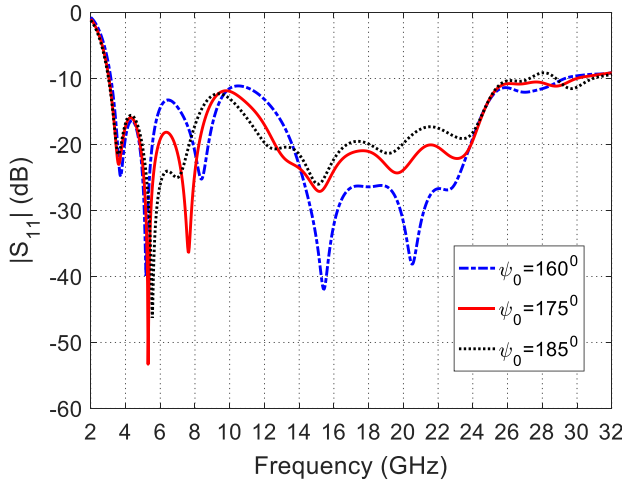

Figure 4. Effect of varying the flare angle parameter, Ψ_0, on the frequency response of $|S_{11}|$.

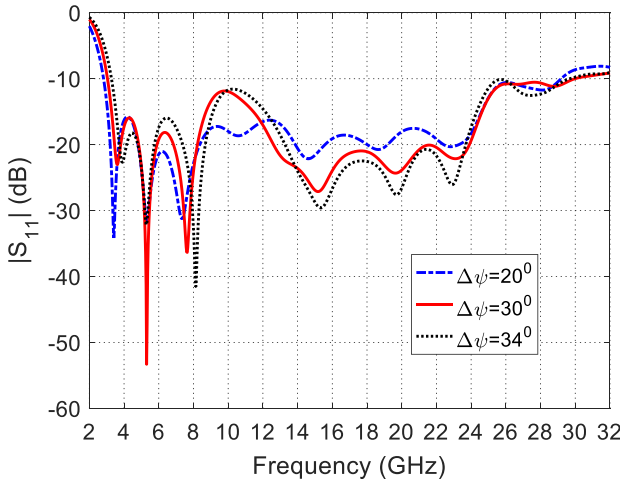

Figure 5. Effect of changing the incremental flare angle, $\Delta\Psi$, on $|S_{11}|$ at the excitation port of the two-arm SWB antenna over the frequency range 2–32 GHz.

The variation of the incremental flare angle, $\Delta\Psi$, affects the frequency response of $|S_{11}|$ as shown in Figure 5. It is clear that both the start and end of the frequency band are affected by varying $\Delta\Psi$. To get the largest bandwidth over which $|S_{11}| \leq -10\,\text{dB}$, it is required to set $\Delta\Psi = 30°$.

It may be worth to note that the parametric studies presented above are some examples of the complete parametric studies that have been performed to arrive at the optimum antenna design whose dimensions are presented in Table 1.

3. ANTENNA FABRICATION AND MEASUREMENT

The two-arm SWB antenna is manufactured using the dimensions given in Table 1. The fabricated antenna and the standard coaxial connector attached to the two-arm structure through the proposed balun are presented in Figure 6(a). Figure 6(b) shows the measurement of the reflection coefficient S_{11} by the vector network analyzer (VNA) model ZVA67. Figure 7 shows the frequency dependence of $|S_{11}|$

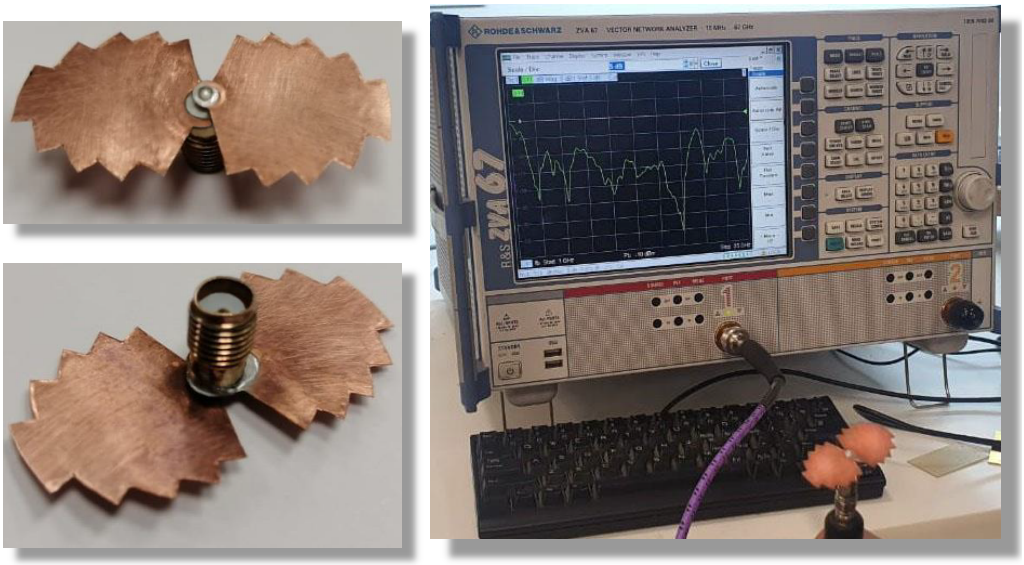

(a) (b)

Figure 6. Measurement of S_{11} at the antenna port using VNA. (a) The fabricated antenna. (b) Measurement setup.

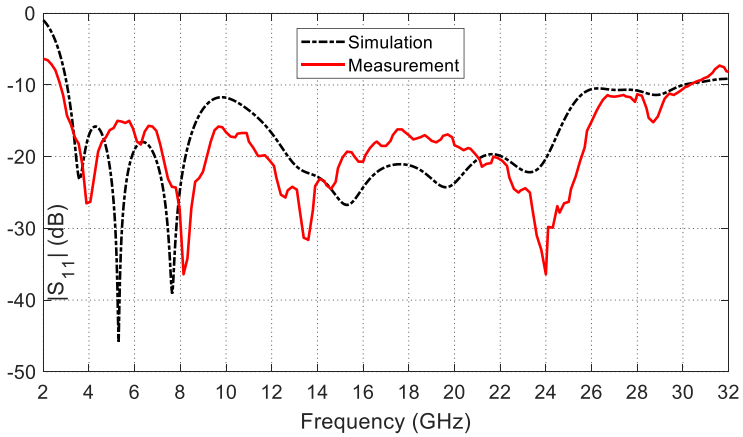

Figure 7. Frequency behavior of the reflection coefficient magnitude, $|S_{11}|$, obtained by simulation and measurement.

as obtained by measurements and simulation. Both the simulation and the measurement results show that the antenna impedance is matched ($|S_{11}| < -10$ dB) over the desired frequency range 3–30 GHz.

4. CURRENT DISTRIBUTION AND FAR FIELD PATTERNS

In this section, the current distributions on the antenna surface and the radiation patterns obtained by simulation are presented and validated by experimental measurements. Also, the method applied to the measurement of far field patterns is described in detail.

4.1. Current Distribution and Radiation Patterns

The surface current distributions on the antenna surface and the far field patterns at different frequencies over the frequency range (3–30 GHz) are presented and discussed in this section.

4.1.1. Current Distribution on the Antenna Surface

To understand the mechanisms of radiation of the proposed two-arm antenna over the wideband (3–30 GHz), it may be useful to investigate the current distributions on the antenna surface at different frequencies over the entire bandwidth. In Figure 8, it is shown that the current patterns on the arm surface show increase of the mode order with increasing the frequency over the operational bandwidth. Figure 8(a) presents surface current pattern at the start of the frequency band (3 GHz). This pattern indicates the excitation of a first-order mode on the antenna arms near this frequency. The surface current patterns presented in Figures 8(b), 8(c), and 8(d) indicate the excitation of second-order, third-order, and fourth-order modes near the frequencies 3, 13, 24, and 30 GHz, respectively. This is attributed to the increase of the electrical length of the antenna arms with increasing the frequency thereby allowing the excitation of higher-order modes with increasing order.

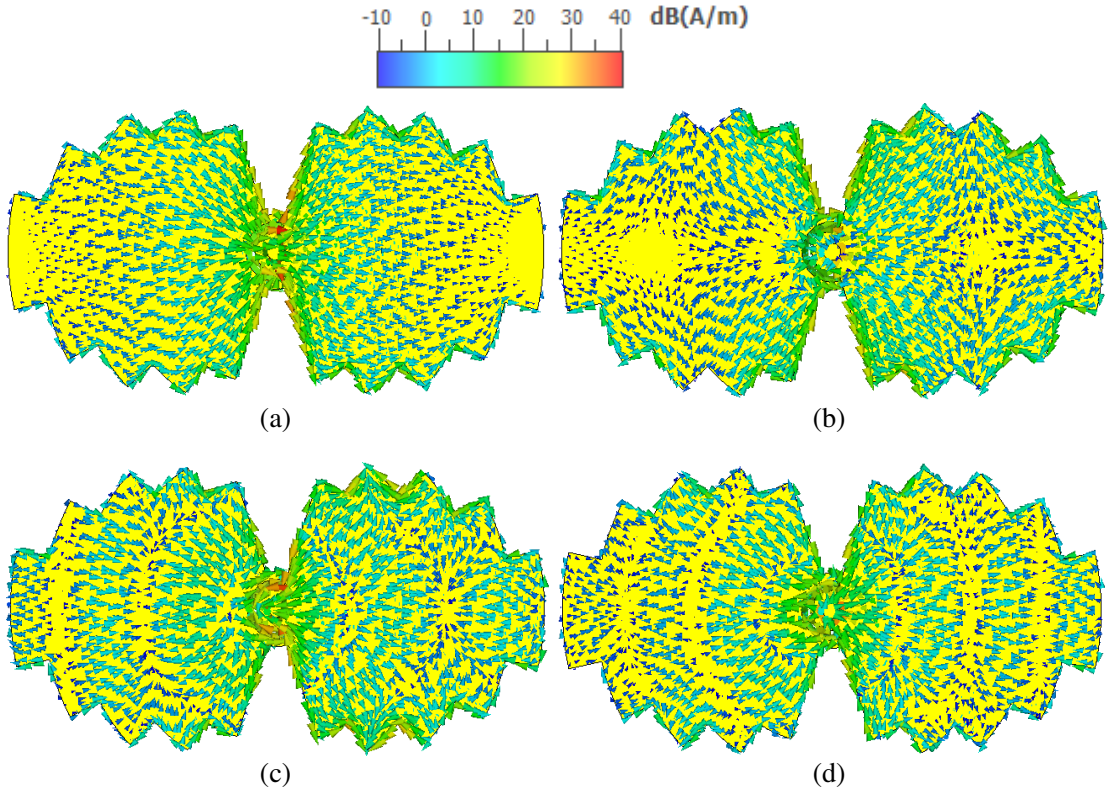

Figure 8. Surface current distribution at the frequencies: (a) 3 GHz, (b) 13 GHz, (c) 24 GHz, and (d) 30 GHz.

4.1.2. Radiation Patterns

As mentioned before, the antenna is proposed for omnidirectional radiation. The azimuth plane is the yz-plane ($\phi = 90°$), and the elevation planes are all the planes containing the longitudinal axis of the antenna (x-axis). Herein, the xy-plane ($\theta = 90°$) is selected for plotting the elevation patterns. The azimuth and elevation patterns of the far field are presented in Figure 9. For convenience while comparing the levels of the radiated field at the different frequencies and in different planes, all the azimuth and elevation radiation patterns are normalized to the same value, which is the maximum radiated field over all the directions in the three-dimensional space and over all the frequencies. It is clear that the radiation is omnidirectional, i.e., nearly uniform in the azimuth plane ($\phi = 90°$) with figure-of-eight pattern in the elevation plane ($\theta = 90°$). Near the start and stop frequencies of the impedance matching band (3 and 30 GHz), the azimuth patterns of the far filed (in the plane $\phi = 90°$) are nearly uniform with quasi-circular symmetry. Near the middle of the impedance matching frequency band (10 and 17 GHz), the radiation pattern is more directive at $\theta = 180°$. In the elevation plane, $\theta = 90°$, the far field patterns exhibit figure of eight at most of the operational band except for the frequencies near 30 GHz at which the antenna produces quasi-isotropic radiation that is nearly uniform in both the azimuth and elevation planes.

The variations of the radiation patterns with varying the frequency over the operational bandwidth can be attributed to the variation of the surface currents excited on the antenna surface as discussed in Section 4.1.1 and presented in Figure 8. The excitation of higher-order modes with increasing the frequency is responsible for the changes of the radiation patterns presented in Figure 9.

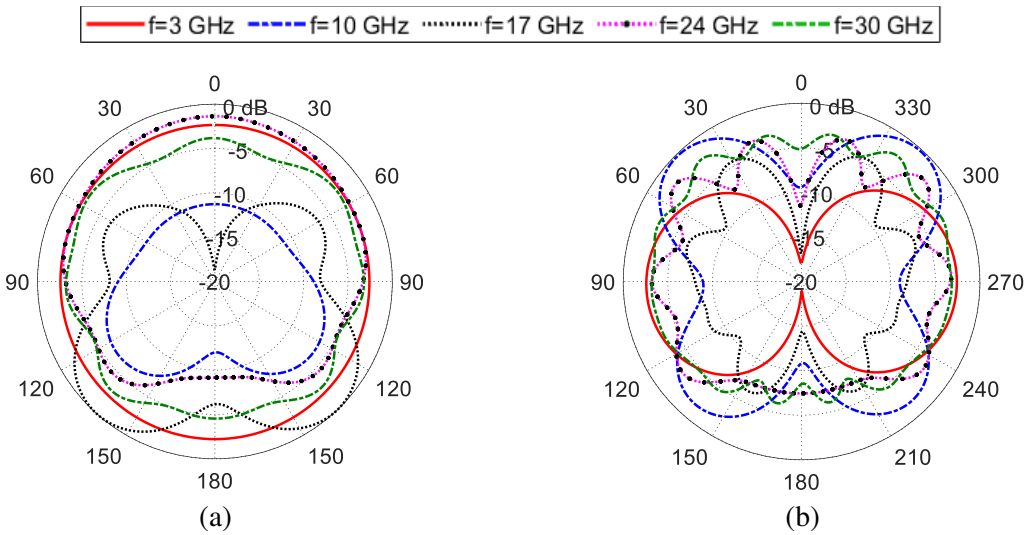

Figure 9. Far field patterns of the proposed antenna (a) in the azimuth plane $\phi = 90°$, (b) in the elevation plane $\theta = 90°$.

4.2. Experimental Assessment of the Far Field Patterns

The results concerned with the far field patterns of the proposed SWB antenna, which have been obtained by simulation, are presented in Section 4.1.2. The experimental results of the measured far field patterns are presented in comparison to patterns obtained by simulation. Also, the method of far field measurement using the VNA is described in detail. Figure 10 shows the far field measurement setup using the VNA and other apparatus. The far field measurement requires a receiving reference antenna (RA) for evaluating the far field produced by the antenna under test (AUT) over the frequency band (3–30 GHz). The RA is maintained oriented towards the AUT that is placed on the rotator. During measurements, the rotator scans the entire space by making complete rotations in two perpendicular planes. The RA and AUT are connected to ports 1 and 2, respectively, of the two-port VNA. During the rotation of the AUT to scan the entire space, the measured values of the parameter S_{21} are uniformly

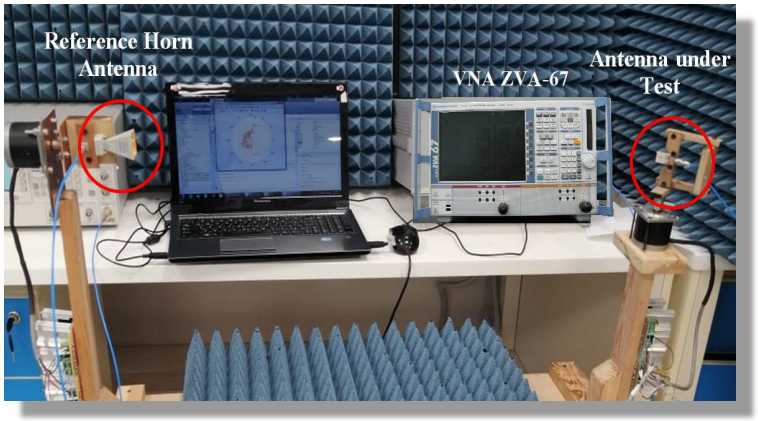

Figure 10. The apparatus sued for measuring the gain and far field patterns.

acquired at all the frequencies. A program on the laptop controls the VNA and the rotator making the required synchronization and stores the required data. The gain, radiation efficiency, and any other far field quantities can be calculated and plotted at the desired frequencies.

Let G_{REF} be the gain of the RA that is employed as a receiver in the far field measurement setup shown in Figure 10. The effective area of the RA can be calculated using the following formula [12, 13].

$$A_{REF} = \frac{\lambda^2}{4\pi} G_{\mathrm{REF}} \tag{3}$$

where λ is the wavelength.

Consider that the output power of the transmitter is P_0 and that the power reflected back to the transmitter due to the return loss is P_{RL}. Thus, the power accepted by the AUT is $P_A = P_0 - P_{RL}$. The reflected power, P_{RL}, can be calculated by the following formula [12, 13].

$$\frac{P_{RL}}{P_0} = |S_{11}|^2 \tag{4}$$

The actual power input to the AUT feeding port (the accepted power) can be calculated as follows.

$$P_A = P_0 - P_{RL} = P_0 \left(1 - |S_{11}|^2\right) \tag{5}$$

When the rotator orients the AUT to look at the direction (θ, ϕ), the power received by the RA is $P_R(\theta, \phi)$. In this case, let $S_{21}(\theta, \phi)$ be the value of the mutual coupling measured by the VNA. Thus, the received power, $P_R(\theta, \phi)$, can be calculated as follows.

$$\frac{P_R(\theta, \phi)}{P_0} = \frac{|S_{21}(\theta, \phi)|^2}{1 - |S_{22}|^2} \tag{6}$$

where S_{22} is the reflection coefficient at the excitation port of the RA as measured by the VNA.

The normalized pattern of the radiated power in the far zone can be evaluated by the following expression.

$$\hat{P}_R(\theta, \phi) = \frac{|S_{21}(\theta, \phi)|^2}{\max\left(|S_{21}(\theta, \phi)|^2\right)} \tag{7}$$

Let ζ be the free space wave impedance. The electric field in the far zone can be calculated using the following formula [12, 13].

$$|E(\theta, \phi)| = \sqrt{2\zeta P_R(\theta, \phi)} \tag{8}$$

Making use of (6), the far field pattern can be evaluated as follows.

$$|E(\theta, \phi)| = \sqrt{2\zeta} P_0 \frac{|S_{21}(\theta, \phi)|}{\sqrt{1 - |S_{22}|^2}} \tag{9}$$

The normalized pattern of the electric field in the far zone can be given using the following expression.

$$\hat{E}(\theta,\phi) = \frac{|S_{21}(\theta,\phi)|}{\max(|S_{21}(\theta,\phi)|)} \tag{10}$$

4.3. Comparison by the Radiation Patterns Obtained by Measurement and Simulation

The measured patterns of the radiated field at 3 and 30 GHz in the planes $\phi = 90°$ and $\theta = 90°$, respectively, are presented in Figure 11 in comparison to the patterns of the radiated field obtained by CSR® simulator. It is shown that measurements and simulation results come in good agreement. Also, the uniformity of the far filed pattern at 30 GHz in the azimuth as well as the elevation planes is shown in Figures 11(c) and 11(d). It should be noted that the patterns of the radiated field obtained by the CST® simulator are normalized to the maximum radiated field obtained by simulation over all the directions in the entire space at the different frequencies. Also, the measured patterns of the far field are normalized to the maximum radiated field obtained by measurement over all the directions at the different frequencies.

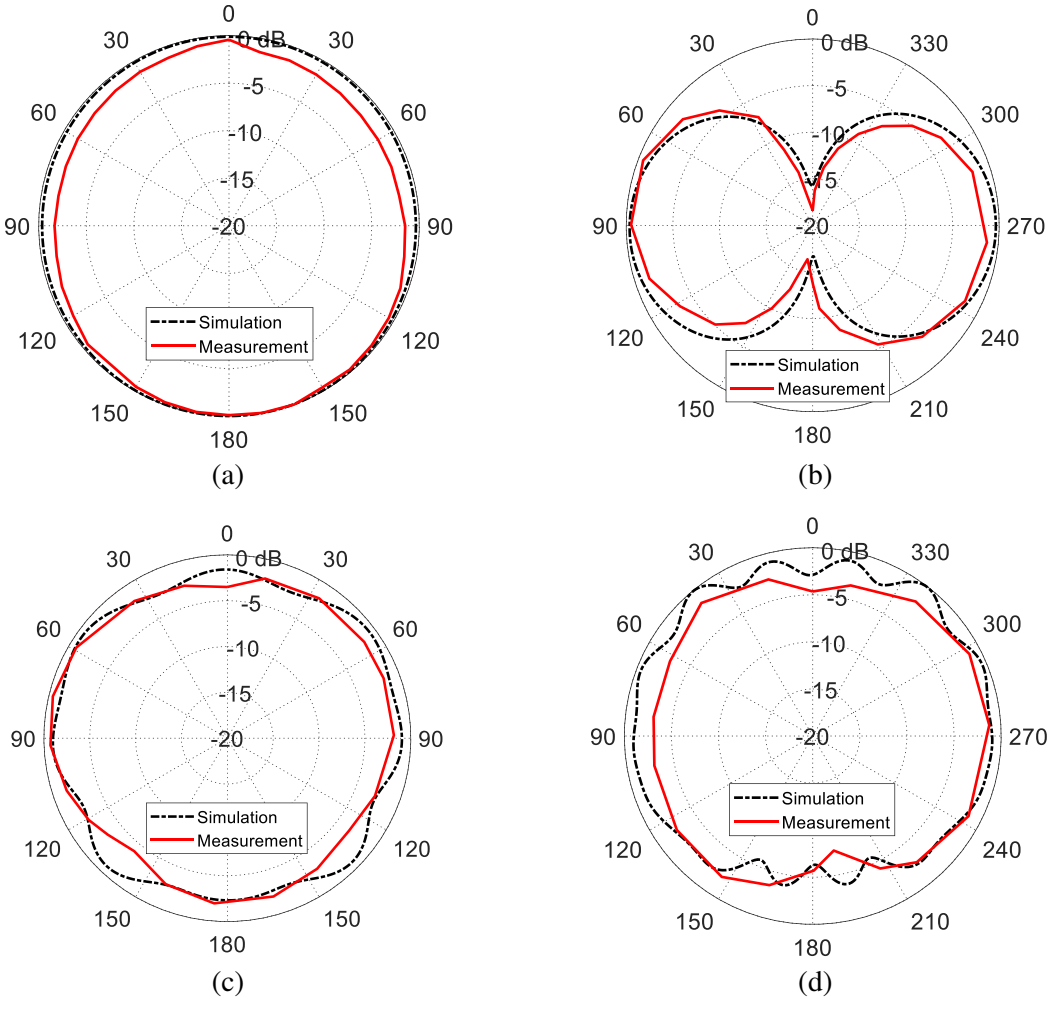

Figure 11. The patterns of the radiated field obtained by simulation compared to the measured patterns for the proposed SWB two-arm antenna (a) at 3 GHz in the plane $\phi = 90°$, (b) at 3 GHz in the plane $\theta = 90°$, (c) at 30 GHz in the plane $\phi = 90°$, and (d) at 30 GHz in the plane $\theta = 90°$.

5. GAIN AND EFFICIENCY MEASUREMENT

The method of measuring the antenna gain and efficiency is described in detail in this section. Also, it presents the simulation and measurements of the far field to show the antenna gain and efficiency over the operational frequency range (3–30 GHz).

5.1. Gain Measurement

Consider that the gain of the AUT in the direction (θ, ϕ) is $G_A(\theta, \phi)$. When the rotator orients the AUT to look at the direction (θ, ϕ), the power density at the RA can be calculated using the following formula [12, 13].

$$\rho\left(\theta, \phi\right) = \frac{P_A G_A(\theta, \phi)}{4\pi D^2} \tag{11}$$

where D is the distance between the AUT and RA.

Consider that the radiation efficiency of the RA is η_{REF}. The power received by the RA antenna when the AUT is oriented at (θ, ϕ) can be evaluated as follows [12, 13].

$$P_R\left(\theta, \phi\right) = \rho\left(\theta, \phi\right) \frac{A_{REF}}{\eta_{REF}} \tag{12}$$

Making use of (11), the power received by the RA can be calculated using the following expression.

$$P_R\left(\theta, \phi\right) = \frac{P_A G_A(\theta, \phi)}{4\pi D^2} \frac{A_{REF}}{\eta_{REF}} \tag{13}$$

Substituting for A_{REF} and P_A from (3) and (5), respectively, into (13), the power received by the RA can be evaluated as follows.

$$P_R\left(\theta, \phi\right) = P_0(1 - |S_{11}|^2) G_A(\theta, \phi) \frac{\lambda^2}{(4\pi D)^2} \frac{G_{REF}}{\eta_{REF}} \tag{14}$$

The gain, $G_A(\theta, \phi)$, of the AUT can be evaluated using the following expression.

$$G_A\left(\theta, \phi\right) = \frac{P_R\left(\theta, \phi\right)}{P_0(1 - |S_{11}|^2)} \frac{(4\pi D)^2}{\lambda^2} \frac{\eta_{REF}}{G_{REF}} \tag{15}$$

Making use of (6), the following formula can be used to calculate the gain of the AUT.

$$G_A\left(\theta, \phi\right) = \frac{|S_{21}(\theta, \phi)|^2}{\left(1 - |S_{11}|^2\right)\left(1 - |S_{22}|^2\right)} \frac{(4\pi D)^2}{\lambda^2} \frac{\eta_{REF}}{G_{REF}} \tag{16}$$

The following expression can be used to calculate the realized gain of the AUT.

$$G_R\left(\theta, \phi\right) = (1 - |S_{11}|^2) G_A\left(\theta, \phi\right) = \frac{|S_{21}(\theta, \phi)|^2}{\left(1 - |S_{22}|^2\right)} \frac{(4\pi D)^2}{\lambda^2} \frac{\eta_{REF}}{G_{REF}} \tag{17}$$

5.2. Measurement of the Antenna Efficiency

The total power radiated by the AUT can be calculated as follows [12, 13].

$$P_{Rad} = \int_0^{2\pi} \int_0^{\pi} \rho\left(\theta, \phi\right) D^2 \sin\theta d\theta d\phi \tag{18}$$

Substituting for $\rho(\theta, \phi)$, expression (18) can be rewritten as follows.

$$P_{Rad} = \frac{4\pi D^2}{\lambda^2} \frac{\eta_{REF}}{G_{REF}} \int_0^{2\pi} \int_0^{\pi} P_R\left(\theta, \phi\right) \sin\theta d\theta d\phi \tag{19}$$

5.2.1. Measurement of the Antenna Total Efficiency

The total efficiency of the AUT can be obtained from (19) as follows [12, 13].

$$\eta_{Total} = \frac{P_{Rad}}{P_0} = \frac{4\pi D^2}{\lambda^2}\frac{\eta_{REF}}{G_{REF}}\int_0^{2\pi}\int_0^{\pi}\frac{P_R(\theta,\phi)}{P_0}\sin\theta d\theta d\phi \tag{20}$$

Making use of (6), the following expression can be used to get the total efficiency of the AUT.

$$\eta_{Total} = \frac{P_{Rad}}{P_0} = \frac{1}{1-|S_{22}|^2}\frac{4\pi D^2}{\lambda^2}\frac{\eta_{REF}}{G_{REF}}\int_0^{2\pi}\int_0^{\pi}|S_{21}(\theta,\phi)|^2\sin\theta d\theta d\phi \tag{21}$$

5.2.2. Measurement of the Antenna Radiation Efficiency

The radiation efficiency is defined by the following expression.

$$\eta_{Rad} = \frac{P_{Rad}}{P_0 - P_{RL}} \tag{22}$$

The definition (22) of the radiation efficiency can be rewritten in the following form.

$$\eta_{Rad} = \frac{P_{Rad}}{P_0}\left(1-\frac{P_{RL}}{P_0}\right)^{-1} \tag{23}$$

Substituting for P_{RL} and P_{Rad} from (4) and (21), respectively, into (23) the radiation efficiency of the AUT can be given by the following expression.

$$\eta_{Rad} = \frac{1}{\left(1-|S_{22}|^2\right)\left(1-|S_{11}|^2\right)}\frac{4\pi D^2}{\lambda^2}\frac{\eta_{REF}}{G_{REF}}\int_0^{2\pi}\int_0^{\pi}|S_{21}(\theta,\phi)|^2\sin\theta d\theta d\phi \tag{24}$$

5.3. Gain and Radiation Efficiency

The proposed antenna gain and radiation efficiency are presented over the frequency range (3–30 GHz). Figure 12(a) shows the dependence of the maximum gain and the gain in the direction ($\theta = 90°, \phi = 90°$)

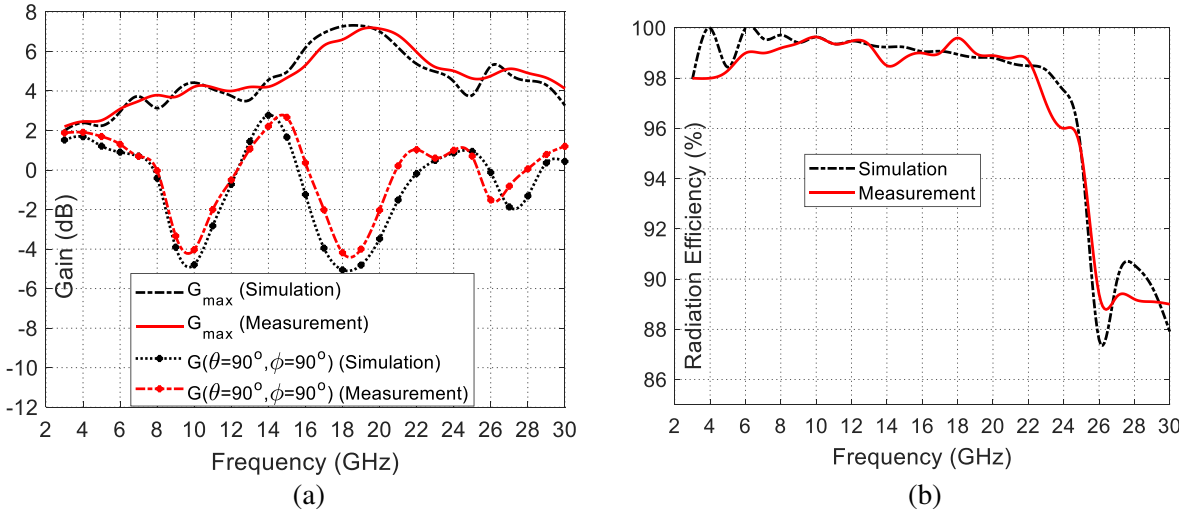

Figure 12. Frequency behavior of (a) the gain and (b) the radiation efficiency of the SWB antenna over the entire frequency band (3–30 GHz).

on the frequency. Figure 12(b) presents the dependence of the antenna radiation efficiency on the frequency. It is shown that the radiation efficiency is greater than 98% over the frequency range (3–22 GHz). Also, the radiation efficiency is greater than 88% over the entire frequency band (3–30 GHz). Good agreement is shown between the measurements and simulation results for both the gain and the radiation efficiency.

6. COMPARISON WITH THE RESULTS OF RECENTLY PUBLISHED WORK

To demonstrate the performance of the SWB two-arm antenna introduced in the present work within the context of other designs with similar objectives, some performance parameters are compared to those presented in some recently literature and listed in Table 2. The comparison is based on some standard measures of the bandwidth including the percentage bandwidth (%BW), RBW, and bandwidth-dimension ratio (BDR). The BDR is defined as follows [14, 15].

$$BDR = \frac{\%BW}{\frac{L}{\lambda_{\max}}\frac{W}{\lambda_{\max}}} \tag{25}$$

where L and W are the antenna length and width, respectively, and $\lambda_{\max}$ is the wave length corresponding to the lowest frequency of the impedance matching bandwidth.

Table 2. List of comparative performance with published planar wideband antenna designs.

Work	Dimensions (mm × mm)	Frequency Range (GHz)	% BW	RBW	BDR	Gain	Radiation Efficiency at Start-End Frequencies
[3]	25.0 × 20.0	3.04–17.39	140.6%	5.7 : 1	2812	4.56	50–73%
[4]	35.0 × 30.0	2.7–28.8	166%	10.7 : 1	1948	NA	96–96%
[5]	28.25 × 30.0	3.4–37.4	167%	11 : 1	1532	6.5	96–60%
[6]	40.0 × 40.0	2.59–31.14	169%	12 : 1	1524	NA	100–92%
[7]	35.0 × 35.0	2.3–34.8	175%	15 : 1	2403	4.76	96–52%
[Present]	40.0 × 21.0	3.0–30.0	164%	10 : 1	1952	5.9	98–88%

7. CONCLUSION

An SWB antenna has been proposed to operate over frequency band (3–30 GHz). This antenna is constructed by merging five sectorial metallic radiators with wide angular dimensions and arc-shaped edges to enhance the bandwidth. Also, a novel wideband balun has been proposed for feeding the two-arm antenna through a coaxial feeder. A prototype has been fabricated for SWB two-arm antenna and subjected to experimental assessment of its performance. The experimental and simulated results concerned with the impedance matching bandwidth, radiation patterns, gain, and efficiency have shown good agreement with each other. The proposed antenna has %BW of 164%, RBW of 10 : 1, and BDR of 1952.

REFERENCES

1. Sagne, D. and R. A. Pandhare, "Design and analysis of inscribed fractal super wideband antenna for microwave applications," *Progress In Electromagnetics Research C*, Vol. 121, 49–63, 2022.
2. Dey, S. and N. C. Karmakar, "Design of novel super wide band antenna close to the fundamental dimension limit theory," *Scientific Reports*, Vol. 10, No. 1, 1–15, 2020.

3. Azim, R., M. T. Islam, H. Arshad, Md. M. Alam, N. Sobahi, and A. I. Khan, "CPW-fed super-wideband antenna with modified vertical bow-tie-shaped patch for wireless sensor networks," *IEEE Access*, Vol. 9, 5343–5353, 2020.
4. Srifi, M. N., O. El Mrabet, F. Falcone, M. S. Ayza, and M. Essaaidi, "A novel compact printed circular antenna for very ultrawideband applications," *Microwave and Optical Technology Letters*, Vol. 51, No. 4, 1130–1133, 2009.
5. Singhal, S. and A. K. Singh, "CPW-fed hexagonal Sierpinski super wideband fractal antenna," *IET Microwaves, Antennas & Propagation*, Vol. 10, No. 15, 1701–1707, 2016.
6. Okan, T., "A compact octagonal-ring monopole antenna for super wideband applications," *Microwave and Optical Technology Letters*, Vol. 62, No. 3, 1237–1244, 2020.
7. Alluri, S. and N. Rangaswamy, "Compact high bandwidth dimension ratio steering-shaped super wideband antenna for future wireless communication applications," *Microwave and Optical Technology Letters*, Vol. 62, No. 12, 3985–3991, 2020.
8. Ouf, E. G., M. A. El-Hassan, A. E. Farahat, K. F. A. Hussein, and S. A. Mohassieb, "Super-wideband two-arm antenna for future generations of mobile communications," *Microwave and Optical Technology Letters*, 2023.
9. Ouf, E. G. E., M. A. E. Abo-Elhassan, A. E. Farahat, K. F. A. Hussein, and S. Mohassieb, "High performance two-arm antenna for super wideband operation," *Progress In Electromagnetics Research C*, Vol. 125, 105–115, 2022.
10. Hussein, K. F. A., "Optimized wideband impedance matching balun for conducting two-arm antennas," *International Journal of Antennas and Propagation*, Vol. 2014, Oct. 2014.
11. Hussein, K. F. A., "Accurate representation of excitation and loading for arbitrarily shaped antennas composed of conducting surfaces in the method of moments," *Progress In Electromagnetics Research B*, Vol. 36, 151–171, 2011.
12. Stutzman, W. L. and G. A. Thiele, *Antenna Theory and Design*, John Wiley & Sons, 2012.
13. Balanis, C. A., *Antenna Theory: Analysis and Design*, John Wiley & Sons, 2016.
14. Nan, J., J. Pan, X. Han, and Y. Wang, "Design of a novel superwideband dual port antenna with second-order Hilbert branches and a modified T-decoupling structure," *International Journal of Antennas and Propagation*, Vol. 2023, 2023.
15. Ayyappan, M. and P. Patel, "On design of a triple elliptical super wideband antenna for 5G applications," *IEEE Access*, Vol. 10, 76031–76043, 2022.